ADEPT: Accurate Diffusion EPI with multi-contrast shoTs

B. Shafieizargar[1,2], B. Jeurissen[1,2], D. H. J. Poot[3], S. Klein[3], J. Van Audekerke[2,4], M. Verhoye[2,4], A. J. den Dekker[1,2], and J. Sijbers[1,2]

[1]imec-Vision Lab, Department of Physics, University of Antwerp, Antwerp, Belgium

[2]µNEURO Research Centre of Excellence, University of Antwerp, Antwerp, Belgium

[3]Biomedical Imaging Group Rotterdam, Department of Radiology and Nuclear Medicine, Erasmus MC, Rotterdam, The Netherlands

[4]Bio-Imaging Lab, Department of Biomedical Sciences, University of Antwerp, Antwerp, Belgium

April 7, 2023

Approximate word count: 150 (Abstract) 5830 (body)

Abstract

Purpose: To introduce a novel imaging and parameter estimation framework for accurate multi-shot diffusion MRI.

Theory and Methods: We propose a new framework called ADEPT (Accurate Diffusion EPI with multi-contrast shoTs) that enables fast diffusion MRI by allowing diffusion contrast settings to change between shots in a multi-shot EPI acquisition (i.e., intra-scan modulation). The framework estimates diffusion parameter maps directly from the acquired intra-scan modulated k-space data, while simultaneously accounting for shot-to-shot phase inconsistencies. The performance of the estimation framework is evaluated using Monte Carlo simulation studies and in-vivo experiments and compared to that of reference methods that rely on parallel imaging for shot-to-shot phase correction.

Results: Simulation and real-data experiments show that ADEPT yields more accurate and more precise estimates of the diffusion metrics in multi-shot EPI data in comparison with the reference methods.

Conclusion: ADEPT allows fast multi-shot EPI diffusion MRI without significantly degrading the accuracy and precision of the estimated diffusion maps.

Keywords: QMRI, Diffusion MRI, Multi-shot EPI, Model-based reconstruction, Phase correction

Introduction

Single-shot EPI is the most commonly used imaging technique for fast in-vivo diffusion MRI (dMRI). However, its low effective bandwidth in the phase encoding direction makes single-shot EPI vulnerable to susceptibility artifacts, resulting in geometric distortions, signal dropout, and limited spatial resolution (1–4). To reduce such artifacts, segmenting the k-space readout in multiple EPI shots (multi-shot EPI) has been proposed as an alternative imaging technique for dMRI (5). The read-out duration of each shot in multi-shot EPI can be much shorter than in single-shot EPI, as only a fraction of the whole k-space, is traversed. Therefore, multi-shot EPI is less affected by geometrical distortions and generally displays a higher effective resolution compared to single-shot EPI (6). However, multi-shot EPI also comes with disadvantages. First, it suffers from a longer acquisition time, which scales with the number of shots. Second, nondiffusive coherent bulk motion during the acquisition of each diffusion-weighted (DW) shot may introduce phase shifts in the voxel signal. Indeed, rigid motion (i.e., global translation and rotation) results in linearly varying phase maps (7), while non-rigid motion, such as brain pulsatile motion, may lead to non-linear phase variations (8). In multi-shot EPI, this phase map changes for each DW shot, which, if not corrected for during image reconstruction from different shots, causes ghosting artifacts in the reconstructed images (9).

Various methods have been proposed to correct for phase-related artifacts in multi-shot dMRI. A common approach is to acquire, for each shot of a multi-shot EPI acquisition, an additional navigator echo that fully samples the central section of the k-space. This navigator echo is acquired immediately before or after the original imaging echo with the same diffusion weighting, thereby assuming that the spins experience the same phase errors in both scans. The navigator scan can then be used to correct the motion-induced phase errors prior to image reconstruction (10). Alternatively, to avoid the acquisition of additional navigator data, the phase map can be estimated retrospectively from the data in a pre-processing step, for example through self-navigated acquisition schemes such as PROPELLER (11, 12), EPIK (13, 14), or interleaved spiral (15). In such schemes, a low-resolution phase map is estimated for each shot from a densely sampled region in the k-space, which is then used to reconstruct artifact-free images. Finally, phase maps corresponding to each segment of the k-space can also be estimated without the need for a densely sampled, central part by using parallel imaging, by using parallel imaging (e.g., SENSE (16) or GRAPPA (17)). Thereby, for each shot of under-sampled k-space data, a complex-valued image is reconstructed, after which the corresponding phase maps are incorporated in the reconstruction of the multi-shot magnitude image to correct for the shot-to-shot phase variations. For example, the multiplexed sensitivity encoding (MUSE) technique (18) uses SENSE reconstructed phase maps (after smoothing) to reconstruct artifact corrected magnitude images from multi-shot data. Extensions of MUSE include macroscopic motion effects (AMUSE, (19)) and 3D multi-band imaging (3D-MS-MUSE, (20)). Similar methods relying on GRAPPA instead of SENSE have also been proposed (9, 21).

Apart from shot-to-shot phase variations, traditional multi-shot EPI dMRI suffers from error propagation caused by a two-step approach in diffusion parameter estimation. In this two-step approach, multiple (phase corrected) DW images are reconstructed from k-space data, after which diffusion parameter maps are estimated by voxel-wise fitting a diffusion model to the reconstructed images. Since this two-step approach lacks a feedback mechanism that connects the image reconstruction step with the final estimation of the parameter maps, image reconstruction errors may propagate into the parameter estimation step, introducing a bias. In non-EPI acquisition schemes, diffusion parameter maps have been estimated directly from k-space data, using so-called model-based reconstruction methods that avoid the intermediate image reconstruction step (22–24). In multi-shot EPI dMRI, model-based reconstruction has also been applied, albeit with a pre-processing step to correct for shot-to-shot phase variations. In this approach, a set of (complex-valued) DW images is reconstructed, for example using parallel imaging reconstruction, from which only the phase maps are retained. Next, the diffusion parameter maps are directly estimated from the k-space data while fixing the image phase maps corresponding with the individual shots to their estimates obtained in the pre-processing step (25, 26). However, for an increasing number of shots segmenting the k-space, parallel imaging reconstruction becomes a highly under-sampled problem, which makes its solution increasingly sensitive to noise. An alternative approach, which is advocated in this paper, is to estimate the shot-by-shot phase maps simultaneously with the diffusion maps of interest.

In this paper, we propose Accurate Diffusion EPI with multi-contrast shoTs (ADEPT). ADEPT is a diffusion parameter estimation framework that combines model-based reconstruction with an innovative image acquisition strategy, called intra-scan modulation. Intra-scan modulation involves the fully flexible variation of contrast settings across k-space segments. Whereas conventional multi-shot dMRI reconstructs individual images from shots encoded with the same diffusion contrast, prior to estimating the diffusion parameters by voxel-wise fitting a diffusion model to the reconstructed images, ADEPT estimates the diffusion parameter maps directly from k-space data composed of shots with each a unique diffusion weighting. Moreover, ADEPT accounts for phase mismatches between the different shots by estimating the phase maps of the individual shots jointly with the diffusion parameters in an iterative procedure, instead of fixing them to values estimated in a pre-processing step (25, 26). Through ADEPT, the flexibility of intra-scan modulation in combination with model-based reconstruction is exploited to substantially improve diffusion parameter map estimation accuracy compared to that of conventional estimation methods. Using Monte Carlo simulations and in-vivo animal studies, ADEPT is evaluated in terms of accuracy and precision and its performance is compared with more conventional multi-shot diffusion estimation frameworks which rely on a pre-processing parallel imaging step for the estimation of the phase maps. Initial findings of this work were presented in (27, 28).

Theory

This section describes the signal model of intra-scan modulated multi-shot diffusion data and introduces the ADEPT framework for joint diffusion and phase parameter estimation.

Diffusion signal model

In what follows, intra-scan modulated, multi-coil, multi-shot imaging is considered, where each shot corresponds to a different diffusion weighting. Then, the measured k-space diffusion data $\boldsymbol{q}_{n,c} \in \mathbb{C}^{n_k \times 1}$ of the c-th coil ($c \in \{1, \cdots, n_c\}$) and n-th shot ($n \in \{1, \cdots, n_s\}$), with n_k the number of k-space samples per shot, n_c the number of coil channels and n_s the total number of shots, is given by:

$$\boldsymbol{q}_{n,c} = \boldsymbol{A}_n \mathscr{F} \boldsymbol{C}_c \boldsymbol{u}_n + \boldsymbol{e} \quad , \tag{1}$$

with $\boldsymbol{u}_n = \{u_{nj}\}_{j=1}^{n_v} \in \mathbb{C}^{n_v \times 1}$ the underlying noise-free, fully-sampled, DW image, defined on the grid points $\boldsymbol{r} = \{r_{xj}, r_{yj}\}_{j=1}^{n_v} \in \mathbb{R}^{n_v \times 2}$, and n_v the number of voxels in the image, $\boldsymbol{A}_n \in \{0,1\}^{n_k \times n_v}$ selecting the k-space points acquired in the n-th shot, $\mathscr{F} \in \mathbb{C}^{n_v \times n_v}$ the Discrete Fourier Transform operator and $\boldsymbol{C}_c \in \mathbb{C}^{n_v \times n_v}$ a diagonal matrix representing the coil sensitivity map of the c-th coil. Furthermore, $\boldsymbol{e} \in \mathbb{C}^{n_k \times 1}$ is an additive noise contribution, modeled as a zero-mean complex-valued Gaussian random variable.

In this work, the diffusion tensor imaging (DTI) model is adopted. According to this model, the diffusion in each voxel is described by a symmetric 3×3 diffusion tensor that is fully characterized by six independent parameters. Let $\boldsymbol{D}_j \in \mathbb{R}^{6 \times 1}$ denote the vector of diffusion tensor parameters of the j-th voxel, whereas $\boldsymbol{D} = \{\boldsymbol{D}_j\}_{j=1}^{n_v} \in \mathbb{R}^{n_v \times 6}$ denotes the full diffusion tensor map to be inferred. Furthermore, let $\boldsymbol{s}_0 = \{s_{0j}\}_{j=1}^{n_v} \in \mathbb{C}^{n_v \times 1}$ denote the complex-valued, non-DW image, which includes a time-invariant phase component caused by scan imperfections, such as B_0 and B_1 field inhomogeneities, chemical shifts, or susceptibility differences (29) which can produce a non-linear phase map and let $\boldsymbol{S}_0 = \{S_{0j}\}_{j=1}^{n_v} \in \mathbb{R}^{n_v \times 1}$ denote the non-DW magnitude image defined as $\boldsymbol{S}_0 := |\boldsymbol{s}_0|$, with $|\cdot|$ the point-wise modulus operator. Assuming rigid coherent small-scale bulk motion during the application of the diffusion sensitizing gradients, with each shot, a linear phase map $\boldsymbol{\phi}_n = \{\phi_{nj}\}_{j=1}^{n_v} \in \mathbb{R}^{n_v \times 1}$ is added to the time-invariant phase map, which varies from shot to shot (7, 30):

$$\phi_{nj} = \theta_{n0} + \theta_{n1} r_{xj} + \theta_{n2} r_{yj} \quad , \tag{2}$$

with θ_{n0} and $(\theta_{n1}, \theta_{n2})$ the offset and slope parameters of the motion-induced phase map, respectively. Finally, let the vector $\boldsymbol{\theta}_n = \{\theta_{np}\}_{p=0}^{2} \in \mathbb{R}^{3 \times 1}$ denote the motion-induced phase map parameters of the n-th shot, and let $\boldsymbol{\theta} = \{\boldsymbol{\theta}_n\}_{n=1}^{n_s} \in \mathbb{R}^{3n_s \times 1}$ denotes the motion-induced phase map parameters of all shots. Based on these modeling assumptions, the

signal intensity of the DW image of each shot can be modeled in each voxel as:

$$u_{nj} = s_{0j} e^{-\boldsymbol{b}_n^T \boldsymbol{D}_j} e^{i\phi_{nj}} \quad , \tag{3}$$

with $\boldsymbol{b}_n = [b_n g_{nx}^2, 2b_n g_{nx} g_{ny}, 2b_n g_{nx} g_{nz}, b_n g_{ny}^2, 2b_n g_{ny} g_{nz}, b_n g_{nz}^2]^T \in \mathbb{R}^{6\times 1}$ the vector containing the independent components of the 3×3 symmetric diffusion weighting b-matrix of the n-th shot, b_n the diffusion weighting factor, and $\boldsymbol{g}_n = [g_{nx}, g_{ny}, g_{nz}]^T$ the diffusion gradient direction. In what follows, the DW image $\boldsymbol{u}_n$ will be expressed as $\boldsymbol{u}_n(\boldsymbol{D}, \boldsymbol{s}_0, \boldsymbol{\phi}_n)$ or $\boldsymbol{u}_n(\boldsymbol{D}, \boldsymbol{s}_0, \boldsymbol{\theta}_n)$ to indicate its functional dependence on $\boldsymbol{s}_0$, $\boldsymbol{D}$, and $\boldsymbol{\phi}_n$ or $\boldsymbol{\theta}_n$, as described by Eq. (2) and Eq. (3).

ADEPT joint parameter estimation framework

ADEPT involves the joint estimation of the complex-valued non-DW image $\boldsymbol{s}_0$, the diffusion parameters $\boldsymbol{D}$, and the linear phase parameters $\boldsymbol{\theta}$ from the multi-shot multi-contrast k-space data, using the least-squares estimator given by:

$$\widetilde{\boldsymbol{D}}, \widetilde{\boldsymbol{s}}_0, \widetilde{\boldsymbol{\theta}} = \arg \min_{\boldsymbol{D}, \boldsymbol{s}_0, \boldsymbol{\theta}} \left(\sum_{n,c} ||\boldsymbol{q}_{n,c} - \boldsymbol{A}_n \mathscr{F} \boldsymbol{C}_c \boldsymbol{u}_n(\boldsymbol{D}, \boldsymbol{s}_0, \boldsymbol{\theta}_n)||_2^2 \right) \quad , \tag{4}$$

The least-squares estimator (4) corresponds with a large-scale non-linear optimization problem which can be solved using the cyclic Block Coordinate Descent (cBCD) method (31). This method allows to split the main problem (4) into two less complex sub-problems that are solved alternately in an iterative scheme. In the first sub-problem, the cost function is minimized with respect to $\boldsymbol{D}$ and $\boldsymbol{s}_0$:

$$\widetilde{\boldsymbol{D}}^{t+1}, \widetilde{\boldsymbol{s}}_0^{t+1} = \arg \min_{\boldsymbol{D}, \boldsymbol{s}_0} \left(\sum_{n,c} ||\boldsymbol{q}_{n,c} - \boldsymbol{A}_n \mathscr{F} \boldsymbol{C}_c \boldsymbol{u}_n(\boldsymbol{D}, \boldsymbol{s}_0, \widetilde{\boldsymbol{\theta}}_n^t)||_2^2 \right) \quad , \tag{4.A}$$

whereas in the second sub-problem, the cost function is minimized with respect to $\boldsymbol{\theta}$:

$$\widetilde{\boldsymbol{\theta}}^{t+1} = \arg \min_{\boldsymbol{\theta}} \left(\sum_{n,c} ||\boldsymbol{q}_{n,c} - \boldsymbol{A}_n \mathscr{F} \boldsymbol{C}_c \boldsymbol{u}_n(\widetilde{\boldsymbol{D}}^{t+1}, \widetilde{\boldsymbol{s}}_0^{t+1}, \boldsymbol{\theta}_n)||_2^2 \right) \quad , \tag{4.B}$$

with t the iteration number.

Since the optimization problems (4.A) and (4.B) are non-convex, proper initialization of the cBCD algorithm is vital to find the global minimum. The optimization is started at $\boldsymbol{D} = \widetilde{\boldsymbol{D}}^t$, $\boldsymbol{s}_0 = \widetilde{\boldsymbol{s}}_0^t$ and $\boldsymbol{\theta} = \widetilde{\boldsymbol{\theta}}^t$, respectively, with $\widetilde{\boldsymbol{D}}^0 = \boldsymbol{D}_{ini}, \widetilde{\boldsymbol{s}}_0^0 = \boldsymbol{s}_{0,ini}$ and $\widetilde{\boldsymbol{\theta}}^0 = \boldsymbol{\theta}_{ini}$ the initial values of the parameters, which are determined in a multi-step approach. First, complex-valued, DW images ($\boldsymbol{v}_n = \{v_n\}_{j=1}^{n_v} \in \mathbb{C}^{n_v \times 1}$) are reconstructed separately for each shot, using the SENSE algorithm. Next, the diffusion parameters and the non-DW magnitude signal in each voxel are estimated from the SENSE reconstructed magnitude images by solving the following least-squares problem:

$$\hat{\boldsymbol{D}}_j, \hat{S}_{0j} = \arg \min_{\boldsymbol{D}_j, S_{0j}} \left(\sum_n ||V_{nj} - S_{0j} e^{-\boldsymbol{b}_n^T \boldsymbol{D}_j}||_2^2 \right) \quad , \tag{5}$$

with $\boldsymbol{V}_n := |\boldsymbol{v}_n|$ and $\boldsymbol{V}_n = \{V_{nj}\}_{j=1}^{n_v} \in \mathbb{R}^{n_v \times 1}$ the magnitude of the SENSE reconstructed images $\boldsymbol{v}_n$. The least-squares estimates obtained are used as initial values in the cBCD approach ($\boldsymbol{D}_{ini}$, $|\boldsymbol{s}_{0,ini}|$). Furthermore, the phase of $\boldsymbol{s}_{0,ini}$ is set equal to zero, whereas the initial values of phase parameters for each shot $\boldsymbol{\theta}_{n,ini}$ are obtained by fitting the model described by Eq. (2) to the phase maps of the individually SENSE reconstructed images in the least-squares sense:

$$\hat{\boldsymbol{\theta}}_n = \arg\min_{\boldsymbol{\theta}_n} \left(\sum_j ||\angle v_{nj} - \boldsymbol{r}_j'^T \boldsymbol{\theta}_n||_2^2 \right) \quad , \tag{6}$$

with $\angle v_{nj}$ the phase of the complex-valued, SENSE reconstructed images in each voxel and $\boldsymbol{r}_j' = [1, r_{xj}, r_{yj}]^T \in \mathbb{R}^{3 \times 1}$.

Methods

This section describes how ADEPT is evaluated as an estimator of diffusion parameters from multi-shot data compared to the reference methods.

Reference methods

The reference methods, to which ADEPT was compared, all estimate the diffusion parameters from intra-scan modulated multi-shot data, while relying on parallel imaging (PI) to correct for shot-to-shot phase variations. These are:

PI-2step follows a conventional two-step parameter estimation approach (32). First, an image is reconstructed from each shot of the intra-scan modulated k-q-space data using the SENSE algorithm. This results in n_s reconstructed DW images in total. Next, the diffusion parameters $\boldsymbol{D}$ and the non-DW magnitude signal $\boldsymbol{S}_0$ are estimated voxel-wise from the SENSE reconstructed magnitude images solving the optimization problem defined by (5).

PI-MB follows a model-based (MB) approach in which the diffusion parameters $\boldsymbol{D}$ and the non-DW image $\boldsymbol{s}_0$ are estimated directly from the intra-scan modulated k-q-space data by solving the following optimization problem:

$$\widetilde{\boldsymbol{D}}, \widetilde{\boldsymbol{s}}_0 = \arg\min_{\boldsymbol{D}, \boldsymbol{s}_0} \left(\sum_{n,c} ||\boldsymbol{q}_{n,c} - \boldsymbol{A}_n \mathscr{F} \boldsymbol{C}_c \boldsymbol{u}_n(\boldsymbol{D}, \boldsymbol{s}_0, \boldsymbol{\phi}_n)||_2^2 \right) \quad , \tag{7}$$

where the phase of $\boldsymbol{s}_0$ is fixed to zero and the phase maps $\boldsymbol{\phi}_n = \{\phi_{nj}\}_{j=1}^{n_v}$ corresponding with the individual shots are fixed to their SENSE reconstructed values, which are obtained in a pre-processing step. This method exploits the ideas behind MUSE (18) and model-based diffusion tensor estimation in multi-shot EPI (25).

PI-lin-MB incorporates the linear phase model described by Eq. (2). Following a model-based approach, the diffusion parameters $\boldsymbol{D}$ and the complex-valued non-DW image $\boldsymbol{s}_0$ are estimated by solving the following optimization

problem:

$$\widetilde{\boldsymbol{D}}, \widetilde{\boldsymbol{s}}_0 = \arg\min_{\boldsymbol{D}, \boldsymbol{s}_0} \left(\sum_{n,c} ||\boldsymbol{q}_{n,c} - \boldsymbol{A}_n \mathscr{F} \boldsymbol{C}_c \boldsymbol{u}_n(\boldsymbol{D}, \boldsymbol{s}_0, \boldsymbol{\theta}_n)||_2^2 \right) , \qquad (8)$$

where the phase parameters $\boldsymbol{\theta}_n$ corresponding with the individual shots are fixed to values estimated in a pre-processing step. In this step, for each shot, the parameters $\boldsymbol{\theta}_n$ are estimated by fitting the linear phase model (2) to the phase map of the corresponding SENSE reconstructed image in the least-squares sense. Note that the thus obtained estimates of the phase parameters correspond with $\boldsymbol{\theta}_{ini}$, as previously introduced.

The introduction of these reference methods allows to evaluate how the different key properties of ADEPT (i.e., model-based reconstruction, incorporation of a linear phase model, joint estimation of phase parameters) contribute to its performance.

Implementation

ADEPT and the reference methods were implemented in MATLAB (33). Problems (4.A), (4.B), (7), and (8) were solved using the trust region Newton algorithm (34) combined with Powell's dog leg method (35). The first- and second-order derivatives of the cost functions were computed using our MATLAB implementation of automatic differentiation. The least-squares problem (5) was solved using the trust-region-reflective algorithm (36). The parallel imaging reconstructions used in initializing ADEPT and in the reference methods were performed using the BART toolbox (37). The coil sensitivity maps ($\mathbf{C}_c$) were estimated from the fully-sampled non-DW k-space constructed using the acquired non-DW shots using the ESPIRiT technique (37, 38).

Experiments

To evaluate the parameter estimation performance of ADEPT and the reference methods in terms of accuracy and precision, Monte Carlo simulation experiments as well as in-vivo experiments were performed.

Simulation experiments

For the simulation experiments, multi-shot multi-coil k-q-space data was generated according to the models described by Eq. (1) and Eq. (3). As ground-truth parameters, 96×96 diffusion tensor maps and a non-DW image were used, which were estimated from a real dMRI dataset (39). The phase map estimated from the non-DW image of the in-vivo dataset was used as the phase of the ground-truth non-DW image $\boldsymbol{s}_0$ to simulate the time-invariant phase effects. The

simulated k-q-space data consisted of 60 DW shots, each with a unique diffusion encoding gradient direction (obtained using electrostatic repulsion (40)) and a constant b-value of 1.15 $ms/\mu m^2$, as well as 16 non-DW shots. For each of the DW shots, a linear phase map was generated according to Eq. (2) to simulate motion-induced shot-to-shot phase variations. The offset ground-truth phase parameter of each shot, θ_{n0}, was drawn from a uniform distribution on the interval $[-\pi, \cdots, \pi]$ and the slope ground-truth phase parameters of each shot, θ_{n1} and θ_{n2}, were drawn from uniform distributions on the interval $[-\pi/\text{FOV}, \cdots, \pi/\text{FOV}]$. These intervals were chosen such that the range of the generated phase values was similar to that observed in the real data analyzed in this work. Furthermore, the number of coils was set to $n_c = 8$ and the coil sensitivity maps estimated from a multi-coil scan (41) were used to simulate the diffusion k-space data.

To construct multi-contrast multi-shot data, first, fully-sampled k-q space data was generated, corresponding with the 60 DW images and 16 non-DW images described above. Next, these data were retrospectively sub-sampled by applying binary masks (cfr. $\boldsymbol{A}_n$ in Eq. (1)) that define the specific k-space trajectories of the shots of an interleaved multi-shot acquisition. Finally, the multi-contrast multi-shot data was corrupted by additive, complex-valued, zero-mean, Gaussian white noise. The noise standard deviation was chosen to obtain the SNR values in the range $[10, \cdots, 30]$, where the SNR is defined in image space as the ratio of the spatial average of the noiseless, fully-sampled, non-DW magnitude image of one coil channel and the standard deviation of the noise (in image space). Considering an n_v point Discrete Fourier Transform, the noise variance in the k-space is derived from the noise variance in the image space by multiplying the latter by n_v (42, 43). For each SNR level, 30 realizations of noisy data were generated for statistical analysis ($n_r = 30$). To evaluate the performance of ADEPT and the reference methods for various multi-shot acquisition schemes, the following two simulation experiments were performed:

Performance assessment for different under-sampling rates In this experiment, each method's performance was evaluated as a function of the under-sampling rate (R), where the latter is defined as the number of shots required to fill one fully-sampled k-space. To this end, datasets with different under-sampling rates were generated. Each dataset consists of 60 DW shots with each a unique diffusion contrast and 16 non-DW shots, where the number of k-space data points per shot, and hence the total number of data points in the dataset, decreases proportionally with the under-sampling rate. To create a dataset with an under-sampling rate R, a set of R mutually exclusive binary sampling masks was generated, where each mask defines a unique sampling trajectory corresponding with one shot in the k-space. Together, the R different masks cover the full k-space. Additionally, each of the masks was complemented with the central line of the k-space, being the only part of the k-space shared by all R masks. The masks were then applied to retrospectively sub-sample the fully-sampled k-space data to create 60 DW shots with each a unique diffusion contrast and 16 non-DW shots. Following this procedure, datasets with under-sampling rates 2, 4, 8, and 12 (i.e., 2-, 4-, 8-, and 12-shot datasets) were generated, which were subsequently corrupted by noise as described above. Next, the diffusion parameters $\boldsymbol{D}$ and the non-DW image $\boldsymbol{s}_0$ were

estimated from each noisy realization of the simulated datasets using ADEPT as well as the reference methods, where only non-background voxels were included in the parameter estimation. These voxels were selected using a brain mask, which was created by thresholding the non-DW image and adding morphological operations to remove spurious non-brain voxels (44). Finally, the mean diffusivity (MD) and fractional anisotropy (FA) metrics were calculated from the estimated diffusion parameters.

Performance assessment for different sampling patterns A simulation experiment was set up to evaluate the effect of including no, one, or four shared central k-space lines on the estimation performance of ADEPT. The experiment was performed for 4-shot and 8-shot data. The sampling masks corresponding to the three sampling scenarios used to create the 4-shot dataset are illustrated in Fig. 1. All datasets were corrupted with Gaussian noise (SNR = 15). Next, ADEPT was used to estimate the diffusion parameters D and non-DW image s_0 from these datasets, where again only voxels within the brain mask from the first experiment were included in the parameter estimation. Finally, the diffusion metrics MD and FA were calculated from the estimated diffusion parameters.

In-vivo experiments

Dataset In-vivo mouse brain DTI experiments were performed on a 7T small animal scanner (PharmaScan 70/16 US, Bruker BioSpin GmbH, Germany), equipped with a linear 4-channel array coil designed for mice. The mice were anesthetized with isoflurane in a mixture of oxygen and nitrogen. The DTI data were collected from 3 mice using a DW spin-echo single-shot EPI pulse sequence with the following imaging parameters: TE = 46.13 ms, TR = 3000 ms, FOV = 18×20 mm^2, acquisition matrix = (108×90), in-plane resolution = (0.17×0.22) mm^2, slice thickness = 0.8 mm, b-value = 0.7 ms/μm^2, diffusion gradient duration $\delta = 2$ ms, and diffusion gradient separation time $\Delta = 8$ ms. A total of 6 b0 images and 64 DW images, each with a unique diffusion gradient direction, were acquired within a total acquisition time of 3.5 minutes. The animal study was approved by the Committee on Animal Care and Use at the University of Antwerp, Belgium (permit number 2014-04 (adapted 2019)). The raw single-shot data was denoised using random matrix theory to increase SNR (45, 46).

Experiments As in the first simulation experiment, the performance of ADEPT and the reference methods was evaluated as a function of the under-sampling rate. To this end, the acquired fully-sampled single-shot in-vivo datasets were retrospectively sub-sampled using sets of sampling masks introduced in section Simulation Experiments to generate 2-, 3-, 4-, 5- and 6-shot datasets. Each dataset consisted of 6 non-DW shots and 64 DW-shots each with a unique diffusion contrast. The sampling trajectory of all mutually inclusive shots in one set was complemented with a shared central line as illustrated in Fig. 1b. The diffusion parameters D and the non-DW image s_0 were estimated from each in-vivo multi-contrast under-sampled dataset using ADEPT as well as the reference

methods (PI-2step, PI-MB and PI-lin-MB). The estimation was performed for the voxels with substantial signal intensity defined by a selection mask with visually selecting the brain region in the non-DW image. Next, the metrics MD and FA were calculated from the estimated diffusion parameters.

Evaluation metrics

To quantify the estimation performance in the simulation experiments, the following metrics were used (47):

- *Estimation error* of an estimated diffusion parameter with respect to its underlying ground-truth value, calculated as $\hat{x} - x$, where $\hat{x}$ is the estimated parameter with ground-truth value x.

- *Bias*, which quantifies the accuracy of an estimator, calculated as $(\bar{\hat{x}} - x)$, with $\bar{\hat{x}}$ the sample mean of the n_r estimates of the parameter x.

- *Standard deviation (std)*, which quantifies the precision of an estimator, calculated as $(\Sigma(\hat{x} - \bar{\hat{x}})^2/(n_r - 1))^{1/2}$.

- *Root mean square error (RMSE)*, which is a combined measure of accuracy and precision, calculated as $(\Sigma_{i=1}^{n_r}(\hat{x}_i - x)^2/n_r)^{1/2}$.

Additionally, the spatial average of bias, std, and RMSE maps were calculated inside the brain region.

The estimation performance in the in-vivo experiments was quantified in terms of the regional RMSE (rRMSE), which was calculated as $(\Sigma_{j=1}^{n'_v}(\hat{x}_j - x_j)^2/n'_v)^{1/2}$, where $\hat{x}_j$ is the estimated parameter in the j-th voxel, n'_v is the number of voxels within the brain region and x_j is the underlying ground-truth value of the estimated parameter. The ground truth parameters for the in-vivo experiments were obtained by solving problem (5) for magnitude images that were reconstructed from the fully-sampled single-shot EPI dataset using the SENSE algorithm.

Results

Simulation study

The estimated MD and FA maps from the simulation experiments, along with their corresponding RMSE values, are illustrated in Fig. 2 and Fig. 3, respectively. The corresponding difference maps are shown in section D of the supplementary file. These figures show the results for ADEPT along with those of the reference methods for 2-, 4-, 8-, and 12-shot datasets for SNR = 15. It can be observed that for the 2-shot data (top rows in Fig. 2 - Fig. 3), all methods estimate the diffusion parameters with a comparably low RMSE. The RMSE increases with the under-sampling rate,

but not for all methods to the same degree. It can be seen that for the 12-shot dataset the results of PI-2step (Fig. 2a - Fig. 3a) and PI-MB (Fig. 2b - Fig. 3b) are highly affected by noise and artifacts with nearly 10 times larger RMSE values compared to the corresponding ones of the 2-shot dataset. In contrast, the parameter maps of PI-lin-MB (Fig. 2c - Fig. 3c) and ADEPT (Fig. 2d - Fig. 3d) are much less corrupted by artifacts and have lower RMSE values. Indeed, for the 12-shot dataset, the RMSE value of MD increases with a factor of about 4 for PI-lin-MB and with a factor of about 3 for ADEPT compared to the 2-shot dataset. Furthermore, it follows from Fig. 2 and Fig. 3 that ADEPT outperforms PI-lin-MB in terms of RMSE (for both FA and MD), which suggests the added value of the joint estimation of the phase maps along with the diffusion parameters.

The superior performance of ADEPT becomes more obvious when plotting the error distributions of the diffusion parameters. Fig. 4 shows these distributions for ADEPT as well as the reference methods for 8-shot datasets simulated with $SNR = 15$, where for each of the 30 noise realizations the estimation errors were averaged over a region of interest in the white matter. It can be observed that the widths of the error distributions corresponding to ADEPT and PI-lin-MB are comparable and substantially smaller than the widths of the error distributions corresponding to PI-MB and PI-2step. This suggests that ADEPT and PI-lin-MB have a superior precision. Furthermore, the ADEPT error distributions are most symmetrical around zero. This suggests that ADEPT outperforms all reference methods in terms of accuracy. This can also be observed in Fig. 5, which demonstrates the performance of all methods as a function of the SNR. The figure shows the average values of the bias, std, and RMSE over the entire brain region for MD (top) and FA (bottom), estimated from the simulated 8-shot dataset. It can be observed that ADEPT estimates MD and FA with a lower bias (Fig. 5a) and lower RMSE (Fig. 5c) compared to PI-lin-MB, whereas both methods perform comparably in terms of precision, with ADEPT slightly outperforming PI-lin-MB for $SNR < 20$.

In the second simulation experiment, the effect of modifying the sampling pattern was investigated. Fig. 6 shows the estimated MD (Fig. 6a and Fig. 6c) and FA maps (Fig. 6b and Fig. 6d) using ADEPT, along with the corresponding bias, std, and RMSE measures. The figure shows the estimated maps using the conventional multi-shot sampling pattern without shared lines, the sampling pattern suggested in the ADEPT estimation framework with one shared central line, and the pattern with four shared central lines. Results are shown for 4-shot (top) and 8-shot (bottom) datasets, which correspond with $R = 4$ and $R = 8$, respectively. It can be observed from Fig. 6 that for the 4-shot datasets, adding shared lines to the sampling patterns hardly increases precision and accuracy, whereas for the 8-shot dataset both bias and precision are substantially increased by adding extra lines, where the difference between adding zero or one line is most significant.

In-vivo study

Fig. 7 and Fig. 8 show the estimated MD and FA maps for subject 1 in the in-vivo study, respectively, along with their corresponding rRMSE values. The corresponding difference maps are shown in section D of the supplementary file. The results for PI-2step, PI-MB, PI-lin-MB, and ADEPT are shown for retrospectively sub-sampled 2-, to 6-shot in-vivo datasets. Table 1 summarizes the results for all three in-vivo scanned subjects, reporting the rRMSE of MD and FA estimation using ADEPT and the reference methods. Similar to the simulation study, for all methods an increasing trend can be found in the rRMSE values as the under-sampling rate increases. Moreover, it is observed that for datasets with $R > 2$, ADEPT outperforms all reference methods in terms of rRMSE for both FA and MD. The figures related to subjects 2 and 3 are provided in the section A of the supplementary file.

Discussion

We introduced ADEPT as a framework that enables fast, phase-corrected multi-shot dMRI by combining a flexible, intra-scan modulated data acquisition strategy with model-based reconstruction. ADEPT efficiently exploits redundancies in the DW multi-shot k-q space data by estimating the diffusion parameter maps directly from the acquired data. It was demonstrated in both simulation and in-vivo experiments that for high under-sampling rates ($R > 2$), ADEPT outperforms reference methods that rely on parallel imaging to correct for phase variations across shots in a pre-processing step. In particular, for such under-sampling rates, ADEPT and PI-lin-MB estimate diffusion parameter maps with a lower RMSE (cfr. Fig. 2, 3, and 5) and rRMSE (cfr. Fig. 7, 8; Table 1) than PI-2step and PI-MB. This superior performance of ADEPT and PI-lin-MB, which becomes more pronounced with increasing under-sampling rate, can be attributed to their capacity to more accurately estimate the phase maps. Moreover, benefiting from the joint estimation of the phase parameters along with the diffusion parameters, ADEPT outperforms PI-lin-MB in terms of RMSE and rRMSE. For $R = 2$, however, PI-2step and PI-MB show a similar (in simulations) or even superior (in in-vivo experiment) performance compared to ADEPT and PI-lin-MB. A possible explanation is that for an under-sampling rate as low as 2, parallel imaging algorithms have been shown to reconstruct the underlying complex-valued image quite accurately (48), which may explain why PI-2step and PI-MB can provide accurate phase-corrected diffusion parameter maps. More specifically, in the case of the in-vivo experiments, PI-2step and PI-MB can correct for possible small-scale non-rigid motion, while PI-lin-MB and the current implementation of ADEPT assume this motion to be rigid. However, for increasing under-sampling rates, the image reconstruction performance of parallel imaging declines rapidly, which explains the observed inferior performance of PI-2step and PI-MB compared to ADEPT and PI-lin-MB for $R > 2$.

13

As can be seen from Fig. 5, which shows the simulation experiments with varying levels of SNR, ADEPT consistentlyperforms better compared to the references methods in terms of bias and RMSE, independent of the SNR. For example, for a dataset with SNR = 15 and $R = 8$ (cfr. Fig. 5), ADEPT outperforms the reference methods PI-2step, PI-MB and PI-lin-MB in terms of the RMSE of MD by a factor of about 7, 6, and 1.5, respectively. Similar results were found for FA estimation, where ADEPT outperforms PI-2step, PI-MB and PI-lin-MB in terms of RMSE, by a factor of about 5, 4, and 1.5, respectively. It can also be observed from Fig. 5 that ADEPT (as well as the reference methods) show a rather abrupt decrease in performance for SNR = 10 compared to SNR = 15. This decrease is caused by the degraded quality of the SENSE reconstructed images at low SNR and high under-sampling rates. Since ADEPT is initialized with parameter estimates obtained from SENSE reconstructed images, a poor SENSE reconstruction quality will directly affect ADEPT's performance. Indeed, for SNR = 10 and under-sampling factor $R = 8$ or $R = 12$, additional results of this experiment reported in section B of the supplementary file show that for some shots the phase parameters of the linear phase model are estimated with a large error from the SENSE reconstructed images, resulting in poor initial estimates for ADEPT. This suggests that ADEPT's initialization strategy at high under-sampling rates and low SNR ($R > 4$ & SNR < 15) can still be improved.

Finally, simulation experiments were performed to evaluate the effect of complementing the sampling pattern of each shot of ADEPT's multi-shot multi-contrast acquisition scheme with additional central k-space lines shared by all shots. The results of these experiments (cfr. Fig. 6) showed that for 4-shot data, the gain in accuracy and precision obtained by adding up to 4 central lines is only marginal, whereas for 8-shot data, a significant gain in terms of RMSE (up to a factor of 4 for FA and up to a factor of 10 for MD) can be obtained by adding these central lines. This observation may be explained by the fact that the non-linear estimation problem considered becomes more and more challenging with an increasing under-sampling rate, up to the point where adding even the smallest piece of information or data can have a huge impact.

It should be noted that ADEPT models the phase map of each shot as the sum of a static component (which is constant across the shots) and a dynamic component (which varies across shots) (29). The static component accounts for the effect of B0 and B1 field inhomogeneities, chemical shift, susceptibility differences, etc. It corresponds with the phase map of the non-diffusion weighted image, which will generally be non-linear. ADEPT estimates this (non-linear) phase map along with the other parameters of interest. Complementarily, the dynamic component of the phase map represents the phase accrued due to (small-scale) motion during the diffusion-encoding. In the current version of ADEPT, the dynamic phase component is modeled by a linear phase model for each shot, which accounts for the effect of rigid motion. We showed that even with such a possibly non-comprehensive additional phase model, the artifacts caused by the shot-to-shot phase inconsistencies are substantially reduced, even in real diffusion MRI experiments. Nevertheless, the impact of non-linear dynamic phase contributions on ADEPT performance has been investigated in section C of the supplementary material. In particular, following a similar approach as in (49), dynamic

phase components were generated that are described by a second-order spatial polynomial with uniformly distributed coefficients. The results show a low sensitivity of ADEPT to moderate nonlinear phase contributions suggested by the literature (49) with only a marginal increase of RMSE compared to the linear case.

Furthermore, the current implementation of ADEPT does not correct for geometrical distortions caused by magnetic field inhomogeneities. The in-vivo multi-shot dataset used in this study was generated by retrospective sub-sampling of single-shot EPI data. Due to the long read-out duration of single-shot EPI, the retrospectively sub-sampled multi-shot data was affected by geometrical distortions to a larger extent than what can be expected for prospectively acquired multi-shot data. However, in a prospectively acquired multi-shot dataset, these distortions are expected to become less significant, as multi-shot EPI acquisition allows for a shorter read-out time per shot. Moreover, in our experiments, the effective value of TE (46.13 ms) was chosen sufficiently small relative to T2 to assume that the differences in TE across the acquired k-space lines can be considered negligible and all lines experience a similar T2-weighting (1, 4, 50). Note that the shorter read-out time of multi-shot EPI compared to single-shot EPI allows the use of shorter echo times, which makes multi-shot EPI less sensitive to artifacts related to T2-decay, as well as phase accruals caused by off-resonant spins (4).

ADEPT can be extended in different directions. First, to fully exploit the increased number of degrees of freedom offered by ADEPT in comparison with traditional data acquisition schemes, the framework can be complemented with statistical experiment design (47), which allows finding the data acquisition settings that maximize the precision of the estimated diffusion parameters for a given acquisition time. Equivalently, guided by statistical experiment design, the additional degrees of freedom of ADEPT may be exploited to achieve a target precision using fewer shots (i.e., less acquisition time) than a conventional multi-shot data acquisition scheme that doesn't include intra-scan modulation. Second, while in the current work ADEPT has been evaluated for Cartesian sampling trajectories and a DTI signal model, ADEPT can be extended to include non-Cartesian acquisition schemes such as rotating EPI (12) and higher-order diffusion models such as diffusion kurtosis imaging (51). Third, ADEPT can be expanded to simultaneous multi-slice (SMS) imaging. To this end, the proposed model-based framework should be modified to allow for slice unfolding exploiting coil sensitivity variations in three directions, using a similar formulation as (20, 52). Note that this framework should still account for different phase variations for each individual shot, since motion effects may vary for different slice locations (53). Fourth, the current implementation of ADEPT does not address macroscopic inter-shot motion as it is expected to be negligible in small anesthetized animal studies. For human data, this macroscopic motion can be of a higher level, which may result in voxel misregistration (19). To address this issue, ADEPT may be extended to account for macroscopic inter-shot motion, which is considered future work. A potential strategy is to extend the signal model with additional parameters that define the motion between the shots and then estimate these motion parameters along with the diffusion and phase parameters, following a similar approach as in (54). Finally, ADEPT's initialization strategy can be improved to make it more robust at both high under-sampling rates and low

SNR. A possible approach could be to denoise the complex SENSE-reconstructed images prior to calculating the phase maps and fitting the linear phase model to these phase maps. Alternatively, the currently used unweighted least squares estimator described by Eq. (6) could be replaced by a weighted least squares estimator to account for the fact that the SENSE-reconstructed phase maps have a non-stationary (i.e., spatially varying) variance (55, 56).

While further research is needed to explore its full potential, the current work has demonstrated that ADEPT can become a highly competitive method for quantitative dMRI. Using a multi-shot EPI acquisition scheme, ADEPT is less sensitive to susceptibility artifacts than single-shot EPI dMRI, which contributes to a higher estimation accuracy. At the same time, ADEPT's intra-scan modulation strategy, especially when complemented with optimal experiment design, allows it to estimate accurate and precise diffusion parameter maps from a limited number of shots, being comparable to the number of images used in a conventional single-shot approach. That is, ADEPT has the potential to provide more accurate diffusion parameter maps than single-shot EPI approaches, while requiring a comparable acquisition time, which is well below the acquisition time of conventional multi-shot EPI approaches that do not include intra-scan modulation. This potential will be further explored in future studies.

Conclusion

We presented ADEPT, a framework that allows accurate and precise estimation of diffusion parameter maps from under-sampled multi-shot EPI data. ADEPT combines a novel image acquisition strategy with a model-based reconstruction approach in which diffusion parameter maps are estimated along with shot-to-shot phase variations. It was shown that ADEPT's combined parameter estimation strategy allows to strongly reduce artifacts caused by shot-to-shot phase variations, especially at high under-sampling rates. Moreover, simulation and in-vivo experiments showed a superior estimation performance (in terms of accuracy and precision) of ADEPT compared to conventional multi-shot EPI methods that rely on parallel imaging for phase correction. Finally, ADEPT enables intra-scan diffusion modulation by allowing individual shots of the multi-shot acquisition to have a different diffusion weighting, thereby substantially increasing opportunities for optimal experiment design.

Acknowledgments

References

[1] Farzaneh F, Riederer SJ, Pelc NJ. Analysis of T2 limitations and off-resonance effects on spatial resolution and artifacts in echo-planar imaging. Magnetic Resonance in Medicine 1990;14:123–139.

[2] Le Bihan D, Poupon C, Amadon A, Lethimonnier F. Artifacts and pitfalls in diffusion MRI. Journal of Magnetic Resonance Imaging 2006;24:478–488.

[3] Mani M, Jacob M, Kelley D, Magnotta V. Multi-shot sensitivity-encoded diffusion data recovery using structured low-rank matrix completion (MUSSELS). Magnetic Resonance in Medicine 2017;78:494–507.

[4] Skare S, Newbould RD, Clayton DB, Albers GW, Nagle S, Bammer R. Clinical multishot DW-EPI through parallel imaging with considerations of susceptibility, motion, and noise. Magnetic Resonance in Medicine 2007; 57:881–890.

[5] Butts K, Riederer SJ, Ehman RL, Thompson RM, Jack CR. Interleaved echo planar imaging on a standard MRI system. Magnetic Resonance in Medicine 1994;31:67–72.

[6] Bammer R, Stollberger R, Augustin M, Simbrunner J, Offenbacher H, Kooijman H, Ropele S, Kapeller P, Wach P, Ebner F, Fazekas F. Diffusion-weighted imaging with navigated interleaved echo-planar imaging and a conventional gradient system. Radiology 1999;211:799–806.

[7] Anderson AW, Gore JC. Analysis and correction of motion artifacts in diffusion weighted imaging. Magnetic Resonance in Medicine 1994;32:379–387.

[8] Miller KL, Pauly JM. Nonlinear phase correction for navigated diffusion imaging. Magnetic Resonance in Medicine 2003;50:343–353.

[9] Ma X, Zhang Z, Dai E, Guo H. Improved multi-shot diffusion imaging using GRAPPA with a compact kernel. NeuroImage 2016;138:88–99.

[10] Jeong HK, Gore JC, Anderson AW. High-resolution human diffusion tensor imaging using 2-D navigated multi-shot SENSE EPI at 7 T. Magnetic Resonance in Medicine 2013;69:793–802.

[11] Pipe JG, Farthing VG, Forbes KP. Multishot diffusion-weighted FSE using PROPELLER MRI. Magnetic Resonance in Medicine 2002;47:42–52.

[12] Wen Q, Kodiweera C, Dale BM, Shivraman G, Wu YC. Rotating single-shot acquisition (RoSA) with composite reconstruction for fast high-resolution diffusion imaging. Magnetic Resonance in Medicine 2018;79:264–275.

[13] Nunes RG, Jezzard P, Behrens TEJ, Clare S. Self-navigated multishot echo-planar pulse sequence for high-resolution diffusion-weighted imaging. Magnetic Resonance in Medicine 2005;53:1474–1478.

[14] Zaitsev M, Zilles K, Shah NJ. Shared k-space echo planar imaging with keyhole. Magnetic Resonance in Medicine 2001;45:109–117.

[15] Liu C, Bammer R, Kim DH, Moseley ME. Self-navigated interleaved spiral (SNAILS): Application to high-resolution diffusion tensor imaging. Magnetic Resonance in Medicine 2004;52:1388–1396.

[16] Pruessmann KP, Weiger M, Scheidegger MB, Boesiger P. SENSE: Sensitivity encoding for fast MRI. Magnetic Resonance in Medicine 1999;42:952–962.

[17] Griswold MA, Jakob PM, Heidemann RM, Nittka M, Jellus V, Wang J, Kiefer B, Haase A. Generalized Auto-calibrating Partially Parallel Acquisitions (GRAPPA). Magnetic Resonance in Medicine 2002;47:1202–1210.

[18] Chen NK, Guidon A, Chang HC, Song AW. A robust multi-shot scan strategy for high-resolution diffusion weighted MRI enabled by multiplexed sensitivity-encoding (MUSE). NeuroImage 2013;72:41–47.

[19] Guhaniyogi S, Chu ML, Chang HC, Song AW, Chen NK. Motion immune diffusion imaging using augmented MUSE for high-resolution multi-shot EPI. Magnetic Resonance in Medicine 2016;75:639–652.

[20] Bruce IP, Chang HC, Petty C, Chen NK, Song AW. 3D-MB-MUSE: A robust 3D multi-slab, multi-band and multi-shot reconstruction approach for ultrahigh resolution diffusion MRI. NeuroImage 2017;159:46–56.

[21] Wen Q, Feng L, Zhou K, Wu YC. Rapid golden-angle diffusion-weighted propeller MRI for simultaneous assessment of ADC and IVIM. NeuroImage 2020;223:117327.

[22] Welsh CL, Dibella EV, Adluru G, Hsu EW. Model-based reconstruction of undersampled diffusion tensor k-space data. Magnetic Resonance in Medicine 2013;70:429–440.

[23] Zhu Y, Peng X, Wu Y, Wu EX, Ying L, Liu X, Zheng H, Liang D. Direct diffusion tensor estimation using a model-based method with spatial and parametric constraints. Medical Physics 2017;44:570–580.

[24] Knoll F, Raya JG, Halloran RO, Baete S, Sigmund E, Bammer R, Block T, Otazo R, Sodickson DK. A model-based reconstruction for undersampled radial spin-echo DTI with variational penalties on the diffusion tensor. NMR in Biomedicine 2015;28:353–366.

[25] Dong Z, Dai E, Wang F, Zhang Z, Ma X, Yuan C, Guo H. Model-based reconstruction for simultaneous multislice and parallel imaging accelerated multishot diffusion tensor imaging. Medical Physics 2018;45:3196–3204.

[26] Mani M, Magnotta VA, Jacob M. qModeL: A plug-and-play model-based reconstruction for highly accelerated multi-shot diffusion MRI using learned priors. Magnetic Resonance in Medicine 2021;86:835–851.

[27] Shafieizargar B, Jeurissen B, Poot DHJ, den Dekker AJ, Sijbers J. Multi-contrast multi-shot EPI for accelerated diffusion MRI. In: 43rd Annual International Conference of the IEEE Engineering in Medicine and Biology Society. Virtual, 2021; 1753.

[28] Shafieizargar B, Jeurissen B, Poot DHJ, Van Audekerke J, Verhoye M, den Dekker AJ, Sijbers J. Accelerated multi-shot diffusion weighted imaging with joint estimation of diffusion and phase parameters. In: European Society for Magnetic Resonance in Medicine and Biology. Virtual, 2021; C1.O2.

[29] O'Halloran RL, Holdsworth S, Aksoy M, Bammer R. Model for the correction of motion-induced phase errors in multishot diffusion-weighted-MRI of the head: Are cardiac-motion-induced phase errors reproducible from beat-to-beat? Magnetic Resonance in Medicine 2012;68:430–440.

[30] Rabanillo I, Sanz-Estébanez S, Aja-Fernández S, Hajnal J, Alberola-López C, Cordero-Grande L. Joint image reconstruction and phase corruption maps estimation in multi-shot echo planar imaging. In: Computational Diffusion MRI. Cham, 2019; 19–27.

[31] Beck A, Tetruashvili L. On the convergence of block coordinate descent type methods. SIAM Journal on Optimization 2013;23:2037–2060.

[32] Truong TK, Guidon A. High-Resolution Multi-Shot Spiral Diffusion Tensor Imaging with Inherent Correction of Motion-Induced Phase Errors. Magnetic Resonance in Medicine 2014;71:790–796.

[33] The Mathworks, Inc., Natick, Massachusetts. MATLAB version 9.5.0.944444 (R2018b), 2018.

[34] Steihaug T. The Conjugate Gradient Method and Trust Regions in Large Scale Optimization. SIAM Journal on Numerical Analysis 1983;20:626–637.

[35] Yuan Y. Conditions for convergence of trust region algorithms for nonsmooth optimization. Mathematical Programming 1985;31:220–228.

[36] Coleman TF, Li Y. On the convergence of interior-reflective Newton methods for nonlinear minimization subject to bounds. Mathematical Programming 1994;67:189–224.

[37] Tamir JI, Ong F, Cheng JY, Uecker M, Lustig M. Generalized Magnetic Resonance Image Reconstruction using The Berkeley Advanced Reconstruction Toolbox. In: ISMRM Workshop on Data Sampling and Image Reconstruction. Sedona, AZ., 2016; C.

[38] Uecker M, Lai P, Murphy M, Virtue P, Elad M, Pauly J, Vasanawala S, Lustig M. ESPIRiT–an eigenvalue approach to autocalibrating parallel MRI: where SENSE meets GRAPPA. Magnetic Resonance in Medicine 2014;71:990–1001.

[39] Collier Q, Veraart J, Jeurissen B, Vanhevel F, Pullens P, Parizel PM, den Dekker AJ, Sijbers J. Diffusion kurtosis imaging with free water elimination: A bayesian estimation approach. Magnetic Resonance in Medicine 2018; 80:802–813.

[40] Papadakis NG, Murrills CD, Hall LD, Huang CL, Adrian Carpenter T. Minimal gradient encoding for robust estimation of diffusion anisotropy. Magnetic Resonance Imaging 2000;18:671–679.

[41] Byanju R, Klein S, Cristobal-Huerta A, Hernandez Tamames JA, Poot DHJ. Study of key properties behind a good undersampling pattern for quantitative estimation of tissue parameters. In: Proceedings of the 27th Annual Meeting of ISMRM. Montreal, Canada, 2019; 4540.

[42] den Dekker AJ, Sijbers J. Data distributions in magnetic resonance images: A review. Physica Medica 2014; 30(7):725–741.

[43] Aja-Fernández S, Pieciak T, Vegas-Sánchez-Ferrero G. Spatially variant noise estimation in MRI: A homomorphic approach. Medical Image Analysis 2015;20:184–197.

[44] Sijbers J, Vanrumste B, Van Hoey G, Boon P, Verhoye M, Van Der Linden A, Van Dyck D. Automatic localization of EEG electrode markers within 3D MR data. Magnetic Resonance Imaging 2000;18:485–488.

[45] Cordero-Grande L, Christiaens D, Hutter J, Price AN, Hajnal JV. Complex diffusion-weighted image estimation via matrix recovery under general noise models. NeuroImage 2019;200:391–404.

[46] Tournier JD, Smith R, Raffelt D, Tabbara R, Dhollander T, Pietsch M, Christiaens D, Jeurissen B, Yeh CH, Connelly A. MRtrix3: A fast, flexible and open software framework for medical image processing and visualisation. NeuroImage 2019;202:116137.

[47] van den Bos A. Parameter Estimation for Scientists and Engineers, John Wiley Sons, Inc., Hoboken, NJ, USA. 2007; 1–273.

[48] Vasanawala SS, Alley MT, Hargreaves BA, Barth RA, Pauly JM, Lustig M. Improved pediatric MR imaging with compressed sensing. Radiology 2010;256:607–616.

[49] Hu Z, Ma X, Truong T-K, Song AW, Guo H. Phase-updated regularized SENSE for navigator-free multishot diffusion imaging. Magnetic Resonance in Medicine 2017;78:172–181.

[50] Giannelli M, Diciotti S, Tessa C, Mascalchi M. Effect of echo spacing and readout bandwidth on basic performances of EPI-fMRI acquisition sequences implemented on two 1.5 T MR scanner systems. Medical Physics 2010; 37(1):303–310.

[51] Jensen J, Helpern J, Ramani A, Lu H, Kaczynski K. Diffusional kurtosis imaging: the quantification of non-gaussian water diffusion by means of magnetic resonance imaging. Magnetic Resonance in Medicine 2005; 53:1432–1440.

[52] Wang X, Rosenzweig S, Scholand N, Holme HCM, Uecker M. Model-based reconstruction for simultaneous multi-slice mapping using single-shot inversion-recovery radial FLASH. Magnetic Resonance in Medicine 2021; 85:1258–1271.

[53] Mani M, Jacob M, McKinnon G, Yang B, Rutt B, Kerr A, Magnotta V. SMS MUSSELS: A navigator-free reconstruction for simultaneous multi-slice-accelerated multi-shot diffusion weighted imaging. Magnetic Resonance in Medicine 2020; 83(1):154–169.

[54] Ramos-Llordén G, den Dekker AJ, Van Steenkiste G, Jeurissen B, Vanhevel F, Van Audekerke J, Verhoye M, Sijbers J. A Unified Maximum Likelihood Framework for Simultaneous Motion and T_1 Estimation in Quantitative MR T_1 Mapping. IEEE Transactions on Medical Imaging 2017;36:433-446.

[55] Gudbjartsson H, Patz S. The Rician distribution of noisy MRI data. Magnetic Resonance in Medicine 1995; 34(6):910–914

[56] Andersen AH. On the Rician distribution of noisy MRI data. Magnetic Resonance in Medicine 1996;36(2):331–333.

List of Figures

List of Tables

		MD					FA			
		PI-2step	PI-MB	PI-lin-MB	ADEPT		PI-2step	PI-MB	PI-lin-MB	ADEPT
	2-shot	0.026	0.047	0.055	0.058	2-shot	0.024	0.025	0.029	0.031
	3-shot	0.20	0.23	0.11	0.10	3-shot	0.18	0.14	0.067	0.046
S1	4-shot	0.29	0.49	0.13	0.12	4-shot	0.31	0.28	0.066	0.061
	5-shot	0.31	0.63	0.19	0.17	5-shot	0.36	0.35	0.11	0.076
	6-shot	0.31	1.20	0.64	0.22	6-shot	0.45	0.45	0.42	0.18
	2-shot	0.089	0.091	0.13	0.10	2-shot	0.022	0.026	0.049	0.044
	3-shot	0.18	0.21	0.17	0.12	3-shot	0.16	0.14	0.10	0.069
S2	4-shot	0.33	0.74	0.22	0.16	4-shot	0.30	0.31	0.18	0.11
	5-shot	0.34	0.71	0.25	0.19	5-shot	0.34	0.35	0.24	0.12
	6-shot	0.32	0.92	0.37	0.21	6-shot	0.38	0.46	0.41	0.23
	2-shot	0.023	0.031	0.037	0.044	2-shot	0.022	0.019	0.023	0.024
	3-shot	0.16	0.20	0.070	0.062	3-shot	0.17	0.12	0.074	0.039
S3	4-shot	0.27	0.51	0.12	0.11	4-shot	0.31	0.28	0.12	0.086
	5-shot	0.28	0.45	0.14	0.11	5-shot	0.31	0.31	0.11	0.095
	6-shot	0.28	0.63	0.15	0.13	6-shot	0.34	0.37	0.28	0.22

Table 1: MD and FA rRMSE values for the in-vivo study for 3 subjects (S1, S2, S3).

(a) No shared central lines

(b) One shared central line

(c) Four shared central lines
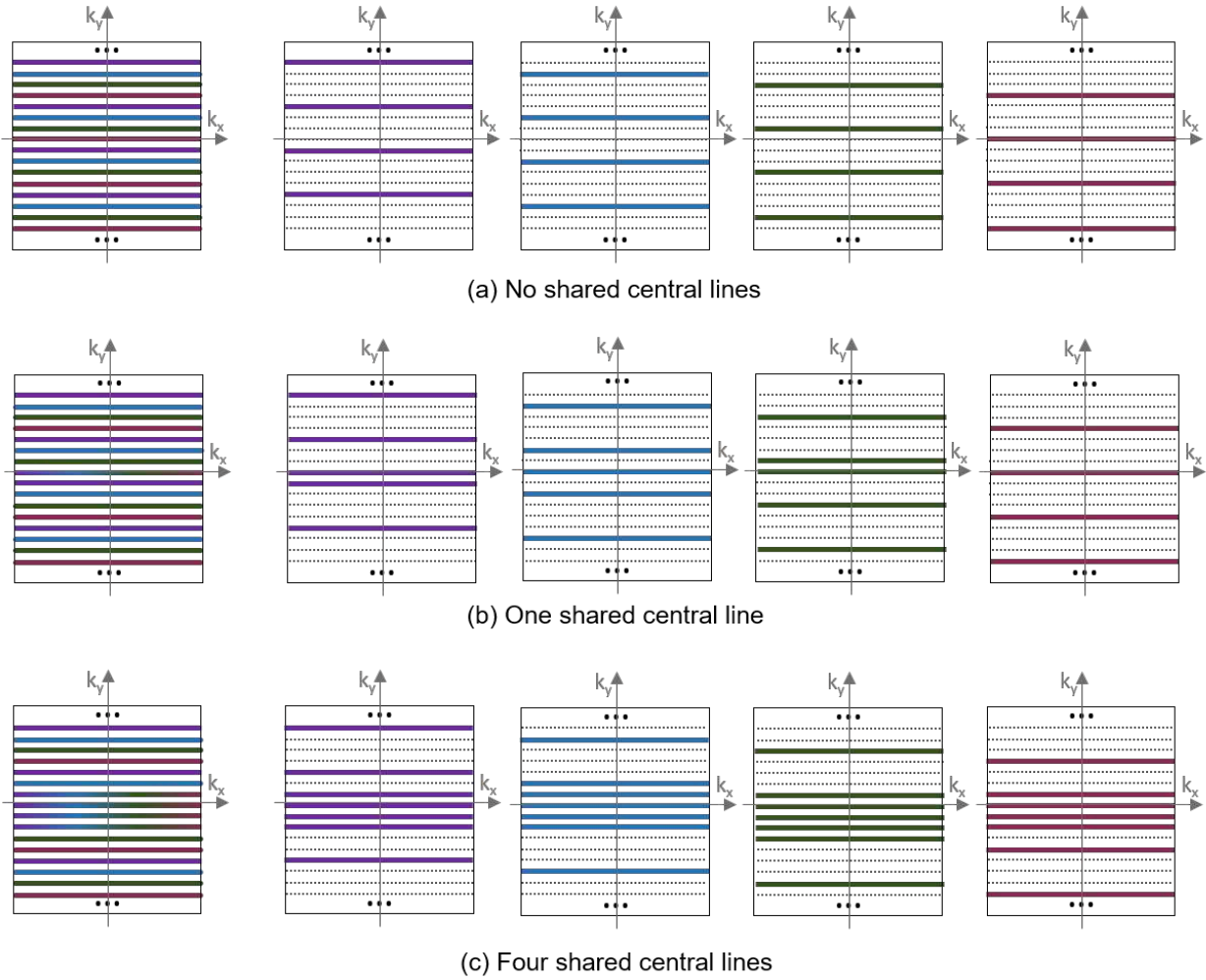
Figure 1: A graphical presentation of the k-space sampling trajectory of the individual shots in a 4-shot EPI acquisition used in simulation experiments. Each shot is acquired with a different diffusion contrast (represented by a different color). Solid lines indicate the sampled points in the k-space, whereas dashed lines indicate the non-sampled points.
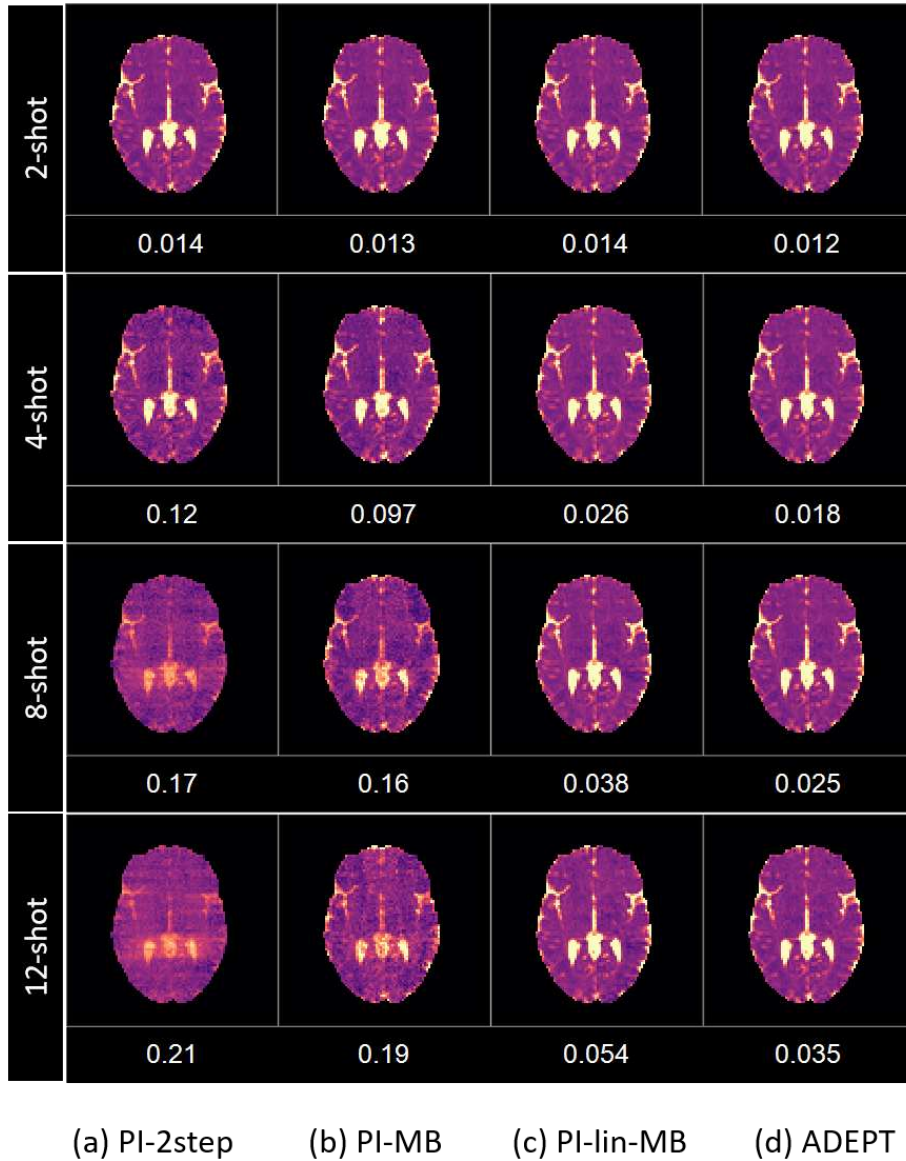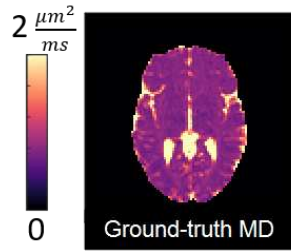
Figure 2: MD maps estimated from simulated multi-shot data with SNR = 15 using PI-2step (a), PI-MB (b), PI-lin-MB (c), and ADEPT (d), along with the corresponding RMSE. From top to bottom row, MD maps estimated from the 2-, 4-, 8-, and 12-shot datasets are shown.
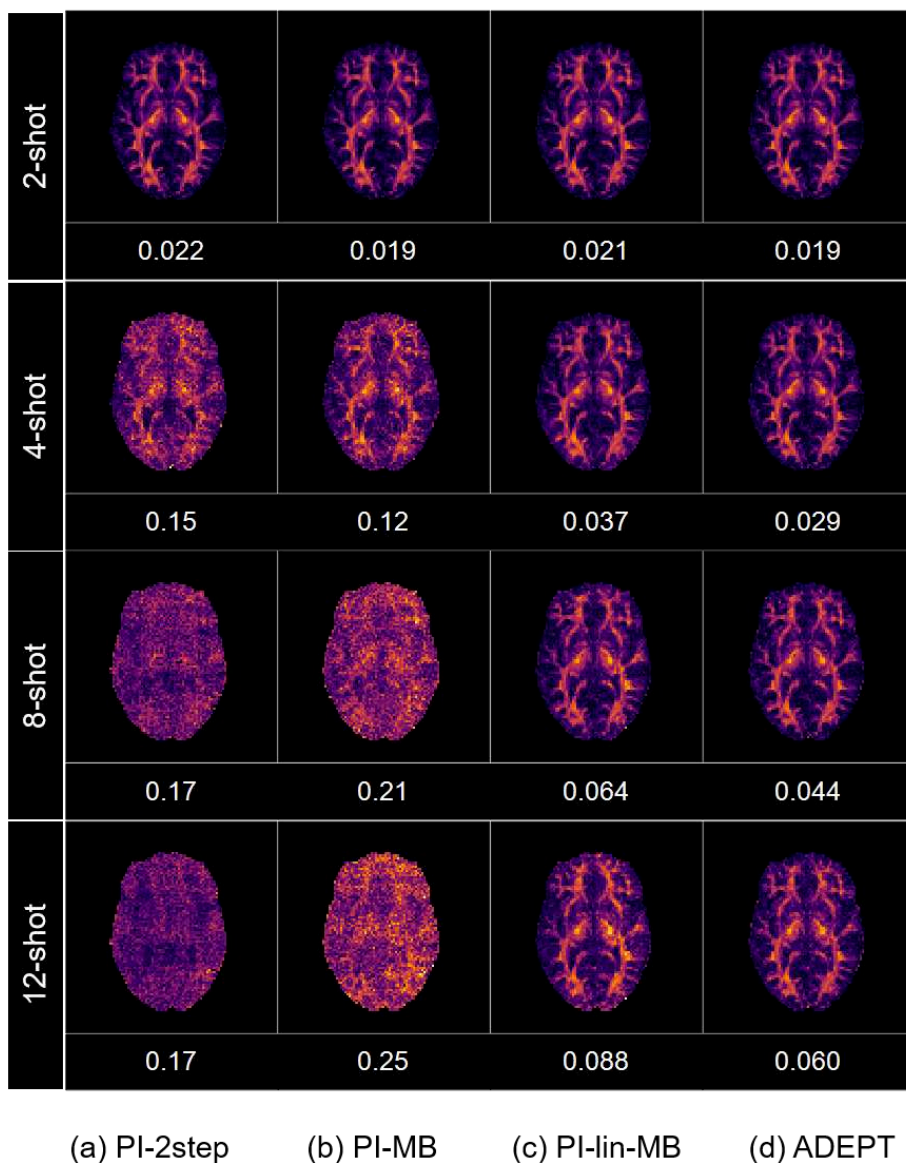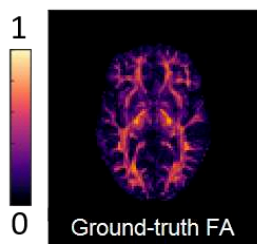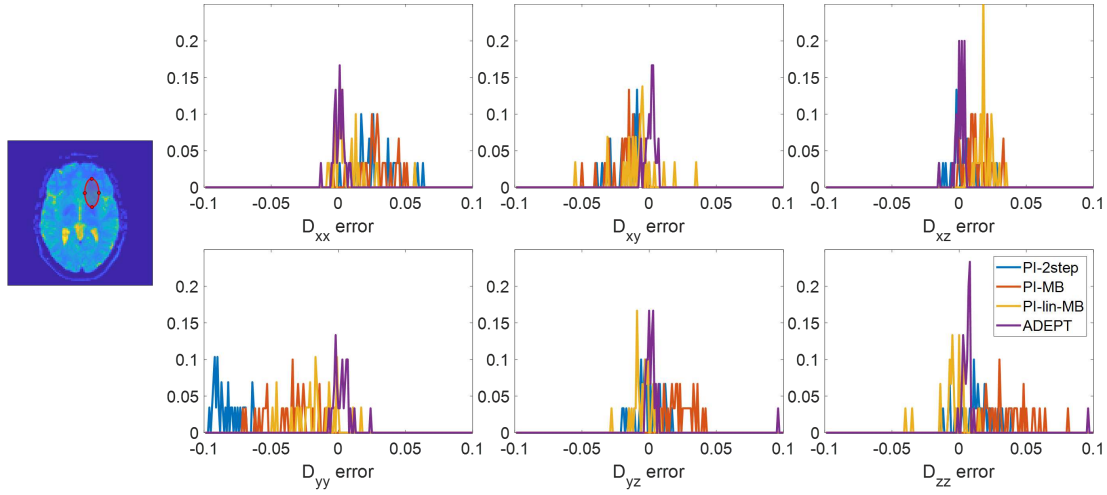
Figure 3: FA maps estimated from simulated multi-shot data with SNR = 15 using PI-2step (a), PI-MB (b), PI-lin-MB (c), and ADEPT (d), along with the corresponding RMSE. From top to bottom row, FA maps estimated from the 2-, 4-, 8-, and 12-shot datasets are shown.

Figure 4: Distribution of the DTI parameter estimation errors for the voxels in the indicated region of interest. The errors are shown for ADEPT and three reference methods in the 8-shot simulation experiment with SNR = 15.
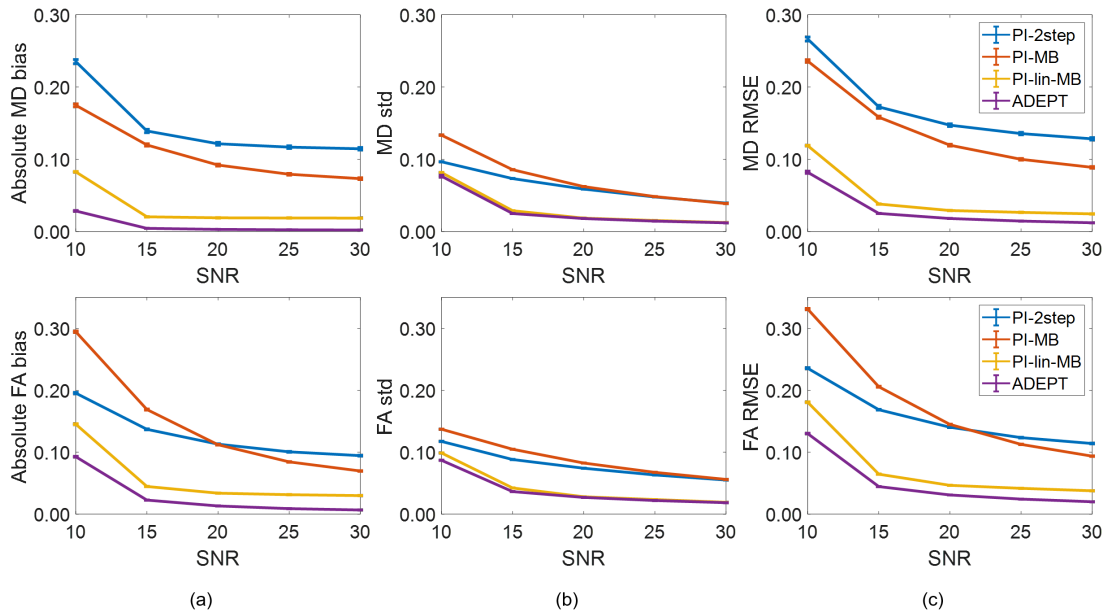

Figure 5: Spatial averages of the absolute bias (a), standard deviation (b), and RMSE (c) maps of MD (top) and FA (bottom), estimated from simulated 8-shot datasets with different SNR values. The error bars correspond to the standard error of the spatial average.
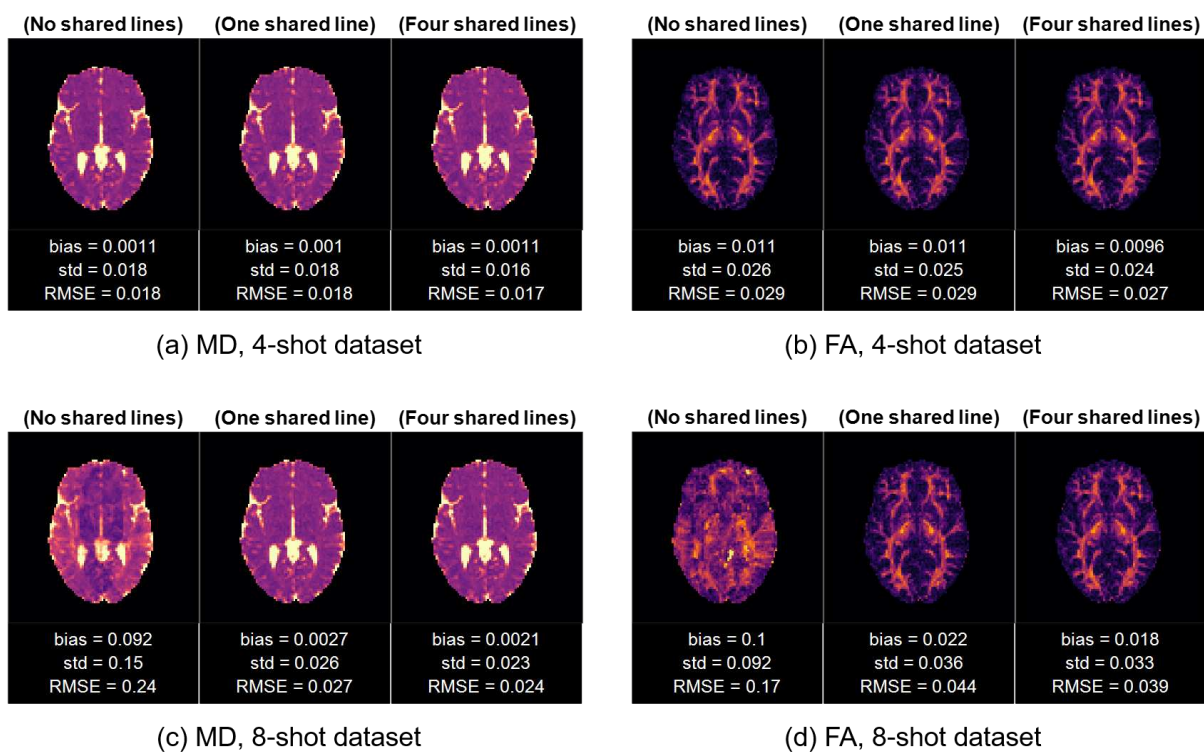
(a) MD, 4-shot dataset

(b) FA, 4-shot dataset

(c) MD, 8-shot dataset

(d) FA, 8-shot dataset

Figure 6: Estimated MD (a,c) and FA (b,d) maps using ADEPT and the corresponding spatial averages of bias, std, and RMSE in the simulation experiments. Results are shown for the 4-shot dataset (top) and the 8-shot dataset (bottom).
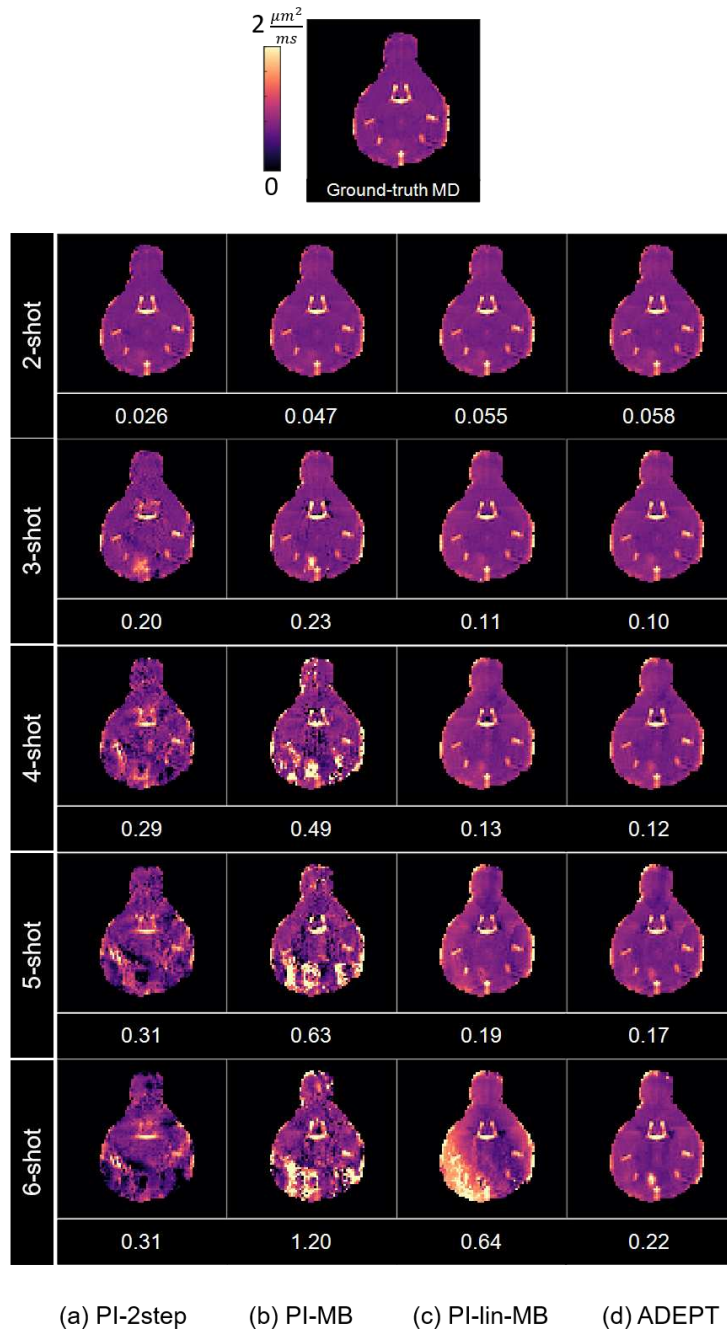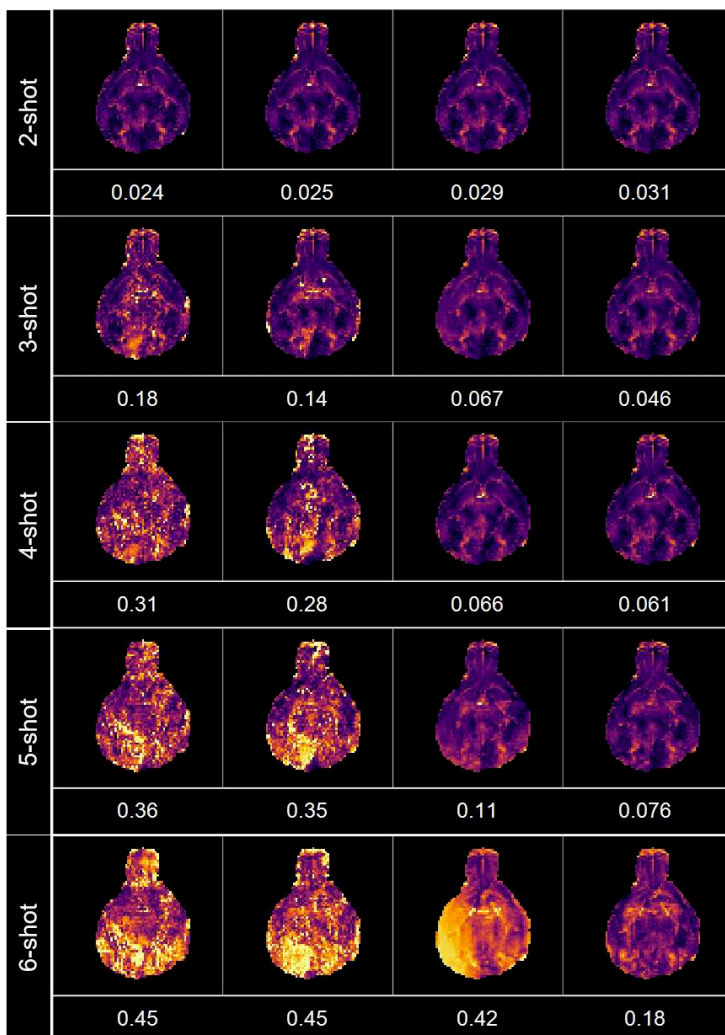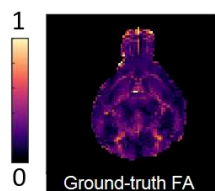
Figure 7: MD maps estimated from the in-vivo dataset using PI-2step (a), PI-MB (b), PI-lin-MB (c), and ADEPT (d), along with the corresponding rRMSE. From top to bottom row, MD maps estimated from the 2-, 3-, 4-, 5-, and 6-shot datasets are shown.

Figure 8: FA maps estimated from the in-vivo dataset using PI-2step (a), PI-MB (b), PI-lin-MB (c), and ADEPT (d), along with the corresponding rRMSE. From top to bottom row, FA maps estimated from the 2-, 3-, 4-, 5-, and 6-shot datasets are shown.